Soils and Rocks

An International Journal of Geotechnical and Geoenvironmental Engineering

www.soilsandrocks.com

ISSN 1980-9743
ISSN-e 2675-5475

The Milton Vargas Lecture 2023 – Shallow tunnels in cohesionless soils: ground behavior and building damage risks

Tarcísio B. Celestino[1]#, Felipe P. M. Vitali[1], Osvaldo P. M. Vitali[2]

Lecture

Keywords
Tunnels
Centrifuge test
Shallow tunnel
Urban tunnel
Numerical modeling
Cohesionless soil

Abstract

The demand for tunnels in densely populated urban areas is growing rapidly to address mobility challenges. Mechanized tunneling is widely adopted in urban environments due to its high productivity and the relatively small ground deformations it induces. However, urban tunneling is highly complex because of the typically shallow depths and interactions with aboveground structures. Therefore, accurately predicting ground deformations induced by mechanized tunneling at the design stage is crucial for assessing potential building damage. To investigate these deformations, a series of centrifuge tunnel tests have been conducted at academic institutions such as the Universities of Cambridge and Nottingham to study the behavior of shallow mechanized tunnels in cohesionless soil. These tests serve as excellent benchmarks for numerical model calibration. Once calibrated to replicate centrifuge test results, numerical models can efficiently analyze a wide range of scenarios at a fraction of the time and cost. This paper investigates ground deformations induced by shallow tunneling in cohesionless soil using numerical models calibrated against selected centrifuge tunnel tests, which encompass varying tunnel diameters, depths, and sand relative densities. The numerical modeling results presented in this paper provide extensive insights into tunnel behavior, illustrating how tunnels respond to different relative densities and depths under tunnel volume losses of up to 5%, approaching failure conditions. Additionally, a comprehensive analysis of ground deformations caused by shallow tunnels in sandy soils and their potential impact on buildings is presented.

1. Introduction

The construction of tunnels in urban areas can induce ground deformations that pose risks to buildings and existing infrastructure. As cities become more densely populated, the demand for tunnels to improve mobility rapidly increases. However, the interaction between tunnels and existing structures in urban environments is highly complex and requires robust numerical modeling for accurate assessment.

Centrifuge tests have been widely used to model tunnel excavation in sandy soils and its interaction with existing geotechnical structures (Marshall, 2009; Farrell, 2011; Zhou, 2015; Franza, 2016; Ritter, 2018; Xu et al., 2021). These tests serve as valuable references for numerical model calibration. Several authors have successfully replicated centrifuge test results through numerical modeling (Boldini et al., 2021; Giardina et al., 2015, 2019; Vitali et al., 2024b,c) and extended the findings to scenarios not explored in physical experiments. Once calibrated, numerical models can efficiently analyze a wide range of conditions at a fraction of the time and cost required for physical testing.

The reliability of numerical models depends on their ability to accurately predict the stresses and strains generated in the ground during tunnel excavation. Tunnel behavior in clayey soils is often undrained, simplifying the problem as volumetric changes typically do not occur in the short term (Mair et al., 1993). However, in sandy soils, volumetric changes occur, significantly increasing the complexity of the problem (Franza et al., 2019; Vitali et al., 2024b).

The ability of numerical models to capture the volumetric strains of sandy soils at different relative densities is crucial for credible modeling of shallow tunnels in sandy soils. In a previous study conducted by the authors (Vitali et al., 2024b), the NorSand model (Jefferies, 1993) was adopted for this purpose. The agreement between experimental and numerical displacements was excellent for tunnel volume losses up to 2.5%. However, the results presented by Vitali et al., 2024b are not valid for tunnel volume losses exceeding 2.5% or for conditions approaching failure. A key limitation of the

---

#Corresponding author. E-mail address: tbcelest@usp.br
[1]Universidade de São Paulo, Escola de Engenharia de São Carlos, Departamento de Geotecnia, São Carlos, SP, Brasil.
[2]University of Hawaii *at Manoa*, Department of Civil, Environmental and Construction Engineering, *Hawaii*, USA.

Submitted on February 13, 2025; Final Acceptance on March 31, 2025; Discussion open until August 31, 2025.

Editor: Renato P. Cunha

https://doi.org/10.28927/SR.2025.003225

NorSand model was that the numerical model reached convergence before failure, even after full stress relief, which is unrealistic. This issue possibly stems from the NorSand constitutive formulation as implemented in commercial FEM software for geotechnical engineering, such as Midas GTS NX and Plaxis, which do not include a dilation cut-off.

This paper investigates ground deformations induced by shallow tunnel excavation in cohesionless soil for tunnel volume losses up to 5% and conditions approaching failure, extending the scope of the previous study by Vitali et al. (2024b). The study is based on numerical models calibrated against selected centrifuge tunnel tests, which consider varying tunnel diameters, depths, and sand relative densities. The behavior of sandy soil at different relative densities was modeled using the well-known Hardening Soil Model (HSM), a widely used constitutive model for soils. The HSM parameters were iteratively derived from triaxial compression and extension tests available in the literature (Lanzano et al., 2016) and from numerical simulations of the selected centrifuge tunnel tests. The developed numerical models successfully replicated centrifuge tunnel test results for tunnel volume losses of up to 5%, capturing soil behavior near failure conditions.

Using a validated numerical model, a set of numerical experiments was conducted, varying tunnel depth and the relative density of sandy soil. These experiments were designed to assess tunnel behavior as it evolves from small tunnel volume losses to very large ones (i.e., a tunnel volume loss of 5%). The findings offer valuable insights into the response of cohesionless ground to tunneling, including volumetric behavior, induced displacements, and potential impacts on aboveground buildings. Additionally, a practical recommendation is provided for estimating horizontal strains at the surface where the maximum principal strain occurs based on the settlement trough, allowing for a more accurate damage assessment during preliminary tunnel design stages.

2. Numerical modeling approach

Numerical modeling replicating the boundary and loading conditions of centrifuge tunnel tests were conducted. The centrifuge tests were performed at the Universities of Cambridge and Nottingham (Marshall, 2009; Farrell, 2011; Zhou, 2015). The selected centrifuge tests for model calibration encompassed various tunnel depths, diameters, and sand relative densities (Dr of 50% and 90%). These tests used Leighton Buzzard Fraction E sand, with maximum and minimum void ratios of 0.97 and 0.64, respectively (Vorster, 2006). Lanzano et al. (2016) carried out an extensive laboratory campaign to investigate the stress-strain behavior of this sand, and their results were used as a reference for calibrating the constitutive model adopted in the numerical simulations.

The well-known constitutive model for soils, Hardening Soil model, was selected to represent the sand's behavior in the numerical simulations. This model is probably the most used in Geotechnical Engineering, and it seems to have reached a reasonable balance between sophistication and practicality.

The Hardening Soil Model is an advanced elastoplastic model based on the Mohr-Coulomb failure criterion. It effectively captures key aspects of soil behavior, including stiffness-stress dependence, shear and compression hardening, and elastic unloading/reloading. Its input parameters can be easily determined from conventional laboratory tests. However, it does not capture strain-softening behavior, which is typically observed in dense sands and highly overconsolidated clays under low confinement stresses. It also does not account for changes in soil relative density, unlike constitutive models based on critical state soil mechanics (e.g., NorSand). Consequently, different constitutive model parameters are required for different relative densities of sand. However, this is not considered a limitation in this study since the numerical results from Vitali et al. (2024b) indicate that the magnitude of the volumetric strains in the soil mass induced by tunnel excavation is minor. Therefore, changes in soil relative density surrounding the tunnel are likely negligible.

The numerical modeling calibration was performed iteratively, considering both the laboratory test results presented by Lanzano et al. (2016) and the selected centrifuge tunnel tests. Figure 1 compares triaxial compression test results on dense sand (D_r = 70%–80%, Figure 1a) and triaxial extension test results on medium-dense sand (D_r = 50%, Figure 1b) with the element test response of the Hardening Soil Model. The figures show the evolution of deviatoric stress (q) and volumetric strain (ε_{vol}) with increments of axial strain (ε_{ax}). Since the triaxial compression tests on dense sand presented by Lanzano et al. (2016) show a slight variation in relative density, a perfect match with the experimental results is not expected. As one can see, the element tests with the calibrated Hardening Soil Model satisfactorily replicated the triaxial test results. Table 1 presents the selected parameters, along with a brief description of each, for relative densities of 50% and 90%.

Figure 2a shows the mesh and dimensions of the numerical models used for this study. The FEM software Midas GTS NX was adopted for numerical analyses. Three centrifuge tunnel tests were selected for validation of the numerical modeling approach: two on dense sand (C/D = 1.33, Farrell 2011, and C/D = 2.44, Marshall, 2009) and one on medium dense sand (C/D = 2.00, Zhou, 2015), with prototype-scale tunnel diameters of 6.15 m, 4.65 m, and 7.2 m, respectively.

The model's dimensions, mesh refinement, and element selection were based on methodologies and recommendations proposed by Vitali et al. (2018a, 2019c, 2021a, 2024a). These approaches were validated by successfully reproducing results from exact analytical solutions (Vitali et al., 2018b; 2019a,b,d; 2020a, b, c; 2021b; 2022b) and accurately modeling actual case histories (Vitali et al., 2019b, 2022a).

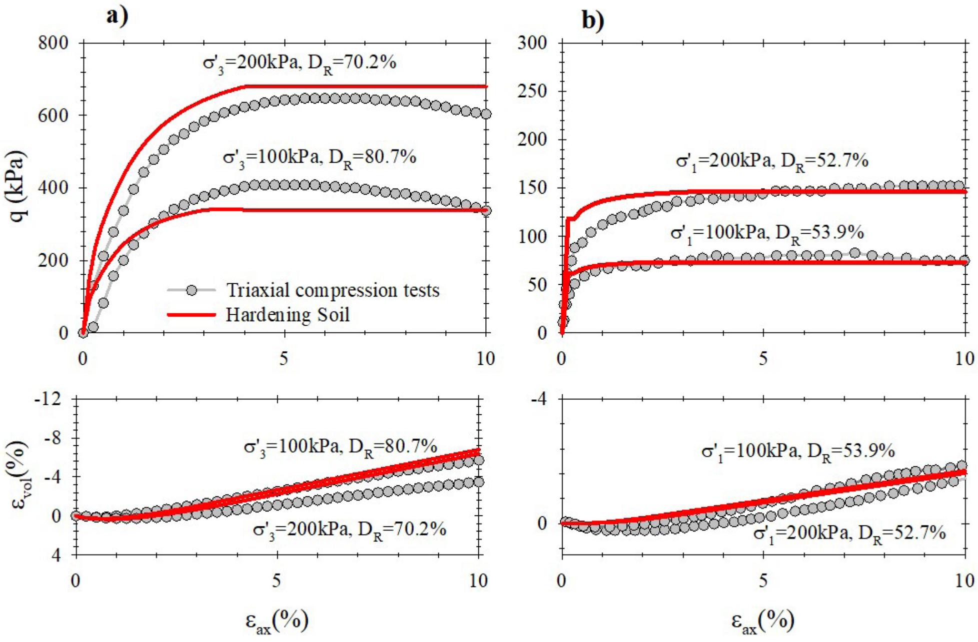

Figure 1. Comparison of the calibrated Hardening Soil model and Lanzano et al. (2016) triaxial test results for (a) drained triaxial compression tests on dense sand; and (b) drained triaxial extension tests on medium dense sand.

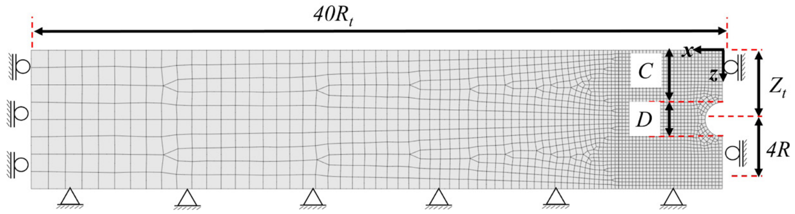

Figure 2. Finite element mesh.

Table 1. Calibrated hardening soil parameters.

Parameter	Definition	D_r = 50%	D_r = 90%
$E_{50,ref}$ (kPa)	Secant Young's modulus in standard drained triaxial test corresponding to p_{ref}	18000	30000
$E_{oed,ref}$ (kPa)	1D compression modulus for primary oedometer loading corresponding to p_{ref}	18000	33000
$E_{ur,ref}$ (kPa)	Unloading / reloading Young's modulus corresponding to p_{ref}.	72000	120000
R_f	Failure ratio	0.85	0.85
p_{ref} (kPa)	Reference stress for stiffness	100	100
m	Power for stress-level dependency of stiffness	0.6	0.6
φ (°)	Friction angle	35	39
$K_{0,NC}$	K_0-value for normal consolidation	0.5	0.5
Ψ (°)	Dilatancy angle	6	17
c (kPa)	Cohesion	0	0
γ_d (kN/m^3)	Dry unit weight	14.6	16
ν_{ur}	Poisson's ratio for unloading-reloading	0.2	0.2
OCR	Overconsolidation ratio	1	1

Half of the model geometry was discretized to leverage the problem's symmetry, applying appropriate boundary conditions at the symmetry plane. The lateral boundaries were placed sufficiently far from the tunnel perimeter to eliminate boundary effects. The model's bottom boundary is located at four tunnel radii (4R) from the tunnel center to minimize buoyancy effects, following the recommendation of Vitali et al. (2019c).

The boundary conditions of the centrifuge tunnel tests were replicated in the numerical models. First, the initial stress state was generated using an at-rest earth pressure coefficient (K_0) of 1-sinϕ (i.e., Jaky's equation). Then, the elements inside the tunnel were deactivated, and nodal forces corresponding to the initial internal pressure of the centrifuge tunnel tests were applied to the tunnel perimeter. Following this step, the displacements were reset, and the imposed nodal forces at the tunnel perimeter were gradually reduced. This reduction in internal stresses at the tunnel perimeter induced stress redistribution and deformations in the surrounding ground. The resulting displacements at the tunnel perimeter were integrated and converted into tunnel volume loss.

Figure 3 presents the evolution of the internal radial stress at the springline normalized with respect to the tunnel's diameter times the soil unit weight ($\sigma_t/\gamma D$) as a function of tunnel volume loss (V_{Lt}). The figure compares results from numerical models and centrifuge tunnel tests. As shown, excellent agreement was observed for the cases where the tunnel cover-to-diameter ratio was 1.33, the relative density was 90% (Figure 3a). Similarly, excellent agreement was found for the case with a cover-to-diameter ratio of 2.0, and relative density of 50% (Figure 3b). For the case with a cover-to-diameter ratio of 2.44, and relative density of 90%, the results showed slight deviations, but the overall agreement remained satisfactory. Notably, most of the stress relief occurred before a tunnel volume loss (V_{Lt}) of 1% to 2% in all three scenarios shown in Figure 3. Beyond this point, large tunnel volume losses occurred with only minor decreases in internal pressure, indicating pronounced nonlinearity and an approaching failure state.

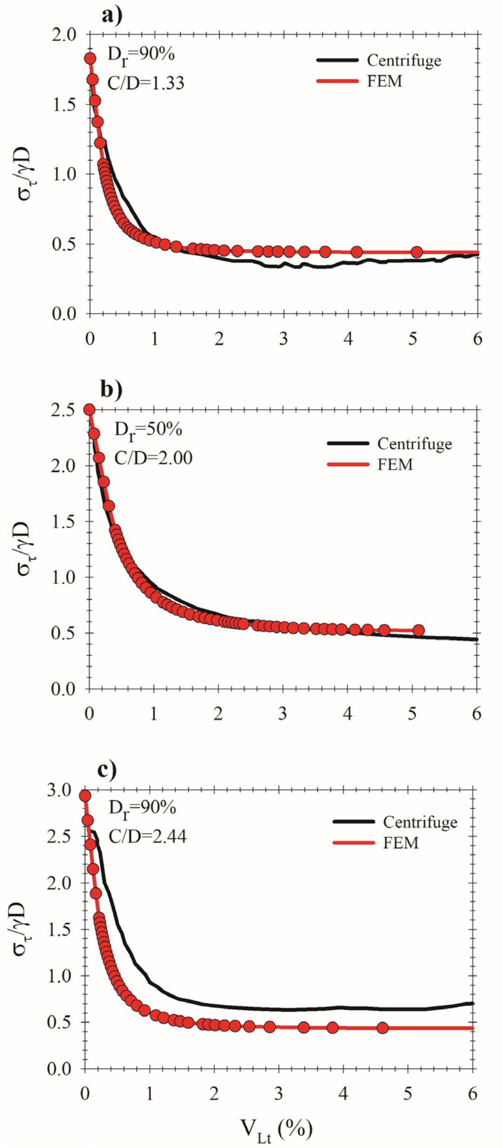

Figure 3. Comparison between centrifuge tests and FEM model, for normalized internal radial stress at springline versus tunnel volume loss, for C/D = 1.33 and D_r = 90% (a), C/D = 2.00 and D_r = 50% (b) and C/D = 2.44 and D_r=90% (c).

Figures 4, 5 and 6 present the vertical displacements at the surface and at a normalized depth of 0.4 times the tunnel depth ($Z = 0.4 \cdot Z_t$, as shown in Figure 2) for a cover-to-diameter ratio of 1.33 and a relative density of 90% (Figure 4), cover-to-diameter ratio of 2.44 and a relative density of 90% (Figure 5), and cover-to-diameter ratio of 2.0 and a relative density of 50% (Figure 6). These figures show the results obtained from centrifuge tunnel tests and numerical models.

In the centrifuge tests, displacements were measured using particle image velocimetry (PIV) techniques, laser sensors, and linear variable differential transformers (LVDTs). As discussed by Vitali et al. (2024b), Marshall (2009), and Zhou (2015), displacements measured with PIV techniques slightly underestimate those recorded by laser sensors and LVDTs, possibly due to friction between the sand and the plexiglass. However, these differences are minor and do not appear to compromise the interpretation of the results.

The results in Figures 4, 5, and 6 are presented with tunnel volume losses up to 5%, which is relatively high given that the expected tunnel volume loss in actual tunnels is typically less than 1%. Both the vertical displacements and the distance from the tunnel centerline are normalized by the tunnel radius. Overall, excellent agreement was observed between the centrifuge tests and numerical models, indicating that the numerical models accurately reproduce the ground deformations observed from centrifuge tunnel tests.

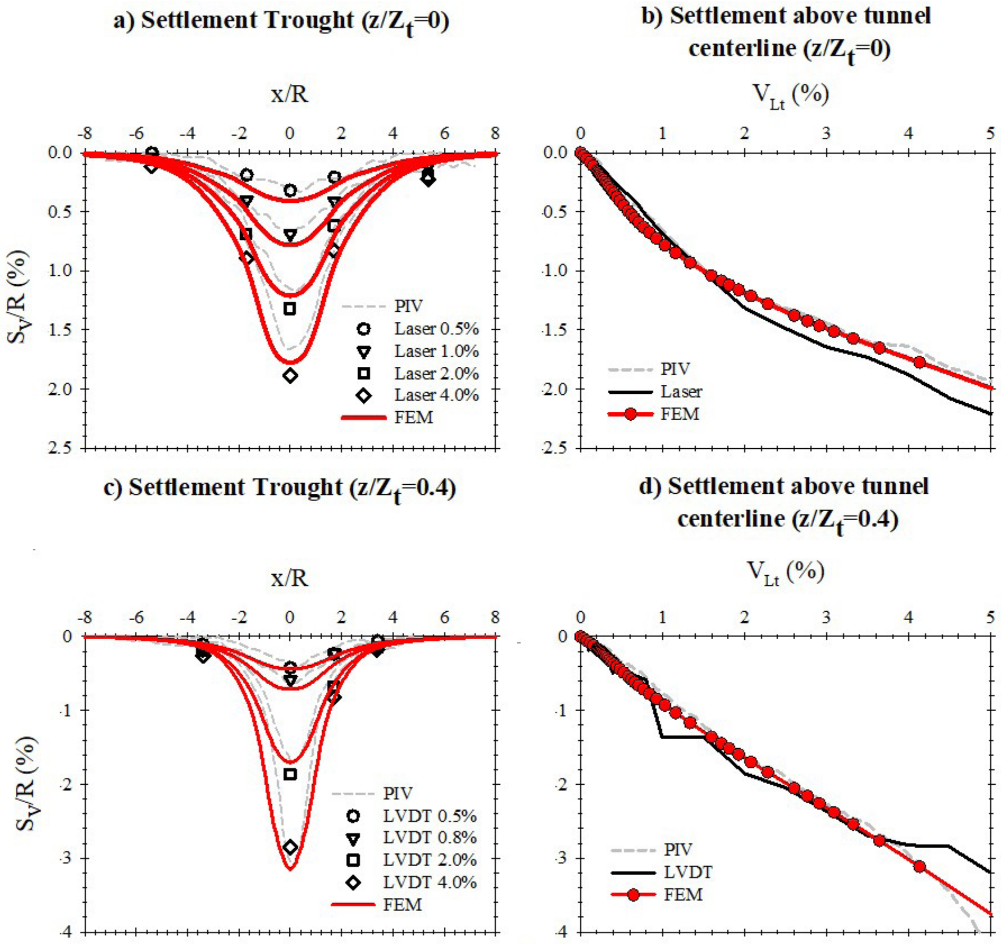

Figure 4. Comparison between FEM results and centrifuge test (*C*/*D* = 1.33 and D_r = 90%). Settlement trough normalized with respect to the tunnel radius (*R*) at: (a) the ground surface, and (c) Z/Z_t = 0.4; and normalized settlement above the crown at: (b) the ground surface, and (d) Z/Z_t = 0.4. The tunnel radius is equal to 3.075 m (i.e., R=3.075 m).

Figures 4a, c, 5a, c and 6a, c show the settlement troughs at the surface and at depth for various tunnel volume losses. As shown in these Figures, the settlement troughs obtained from numerical models are slightly wider than those measured in centrifuge tunnel tests using PIV techniques. However, they align well with the settlement troughs measured by lasers and LVDTs, which are recorded at the mid-length of the strongbox and are, therefore, unaffected by soil friction with the plexiglass interface.

In Figures 4b, 5b, and 5d, which correspond to cases with a relative density of 90%, a nonlinear evolution of the settlement at the centerline above the tunnel is observed as tunnel volume loss increases. As noted by Franza et al. (2019) and Vitali et al. (2024b), dilatancy around the tunnel perimeter during stress relief leads to a nonlinear relationship between settlement and tunnel volume loss by reducing the settlement gradient. Interestingly, this nonlinear behavior is not observed in Figure 4d, which shows settlement at depth for a cover-to-diameter ratio of 1.33 and a relative density of 90%. This may be because the tunnel is too shallow, and the point above the tunnel at a depth of $0.4 \cdot Z_t$ is too close to the tunnel crown.

In Figures 6b and 6d, which correspond to a relative density of 50%, the vertical displacements at the surface and at depth exhibit a less pronounced nonlinear evolution as tunnel volume loss increases compared to cases with a relative density of 90%. This is expected since the dilatancy is smaller, resulting in more linear behavior. As shown by Vitali et al. (2024b) and Franza et al. (2019), this relationship remains linear in loose sands where dilatancy is minor or nonexistent.

3. Effects of relative density and tunnel depth

The influence of relative density and tunnel depth on the mechanics of shallow tunnel excavation in cohesionless soil is investigated through a series of numerical experiments conducted using the validated numerical modeling approach. A circular tunnel with a radius, *R,* equal to 5m is analyzed in sandy soil with relative densities, D_r, of 50% and 90%

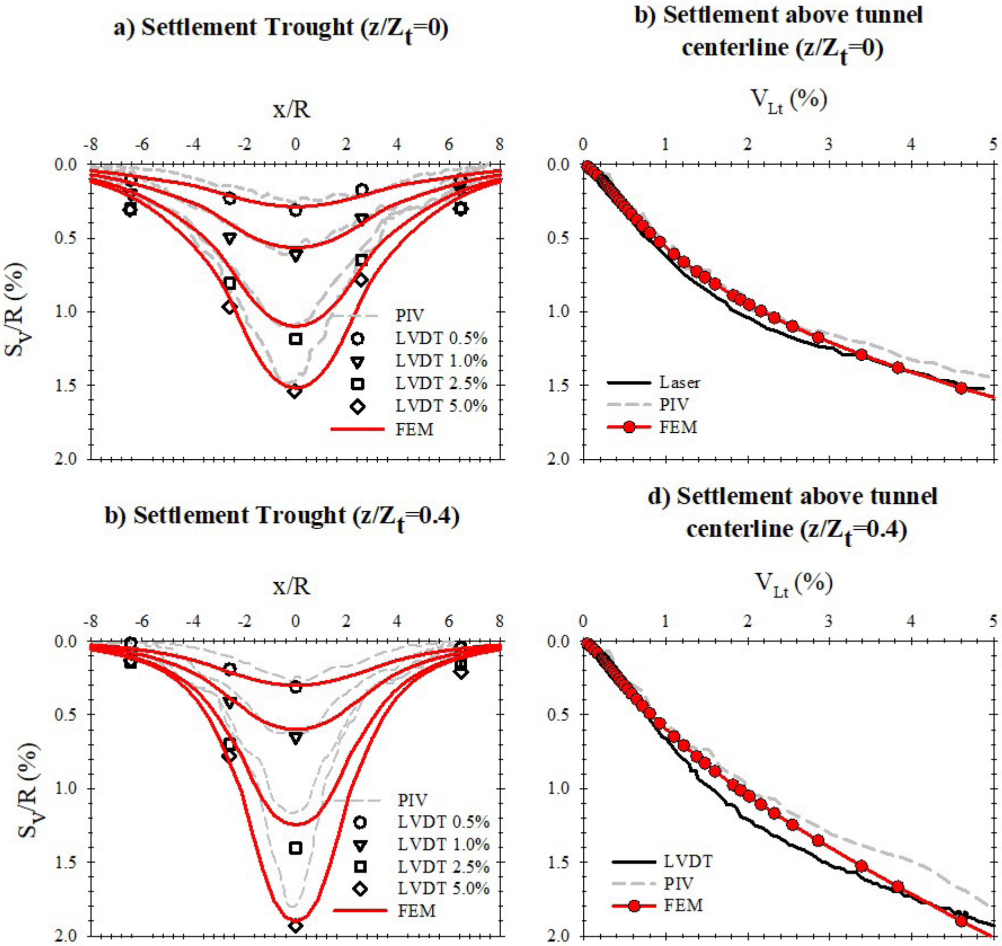

Figure 5. Comparison between FEM results and centrifuge test (C/D = 2.44 and D_r = 90%). Settlement trough normalized with respect to the tunnel radius (R) at: (a) the ground surface, and (c) Z/Z_t = 0.4; and normalized settlement above the crown at: (b) the ground surface, and (d) Z/Z_t = 0.4. The tunnel radius is equal to 2.325 m (i.e., R = 2.325 m).

and cover-to-diameter ratios, *C/D*, of 1.5, 2.0, and 2.5. The selected scenarios are representative of typical shallow tunnels in urban environments.

3.1 Tunnel failure

As discussed in the previous section, the numerical modeling boundary conditions replicate those of the centrifuge tunnel tests conducted by Marshall (2009), Farrell (2011), and Zhou (2015). In these tests, hydrostatic pressure is applied at the tunnel perimeter, with the initial internal pressure at the springline elevation set equal to the overburden stress at that depth. Once stress equilibrium is established, displacements are reset, and the internal pressure is gradually reduced until failure occurs.

Figure 7 illustrates the evolution of normalized internal radial stress ($\sigma_t/\gamma D$) at the springline as tunnel volume loss (V_{Lt}) increases for cover-to-diameter ratios of 1.5, 2.0, and 2.5, with relative densities of 50% (Figure 7a) and 90% (Figure 7b). As shown, the internal radial stress at the tunnel perimeter decreases towards a constant value as the tunnel volume loss increases. The tunnel volume loss required to reach the minimum internal radial stress depends on tunnel depth and the relative density of the sandy ground. The shallower the tunnel and the denser the soil, the smaller the tunnel volume loss needed to reach the minimum internal radial stress.

Atkinson & Potts (1977) proposed a closed-form solution to determine the minimum internal radial stress required at the tunnel perimeter to maintain the stability of an opening in cohesionless ground. Atkinson & Potts's solution indicates that the required minimum internal radial stress is independent of the cover-to-diameter ratio. Consequently, shallower tunnels require less stress relief (i.e., a reduction in initial internal radial stress) to reach the minimum radial stress, which may correspond to failure. Therefore, although the internal pressure at failure remains the same regardless of the cover-to-diameter ratio, a shallower tunnel will collapse before a deeper tunnel, as the stress relief required to reach failure is smaller.

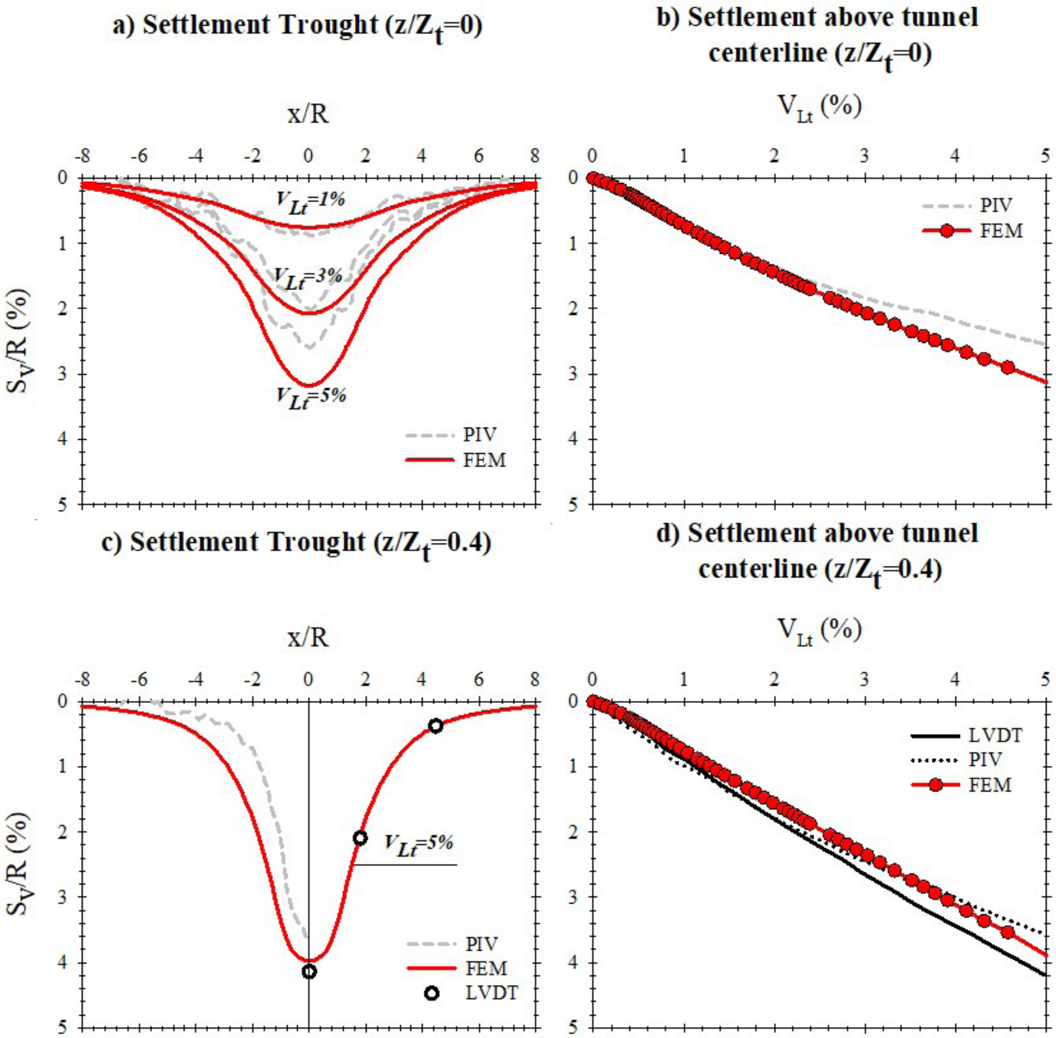

Figure 6. Comparison between FEM results and centrifuge test ($C/D = 2.0$ and $D_r = 50\%$). Settlement trough normalized with respect to the tunnel radius (R) at: (a) the ground surface, and (c) $Z/Z_t = 0.4$; and normalized settlement above the crown at: (b) the ground surface, and (d) $Z/Z_t = 0.4$. The tunnel radius is equal to 3.6 m (i.e., R = 3.6 m).

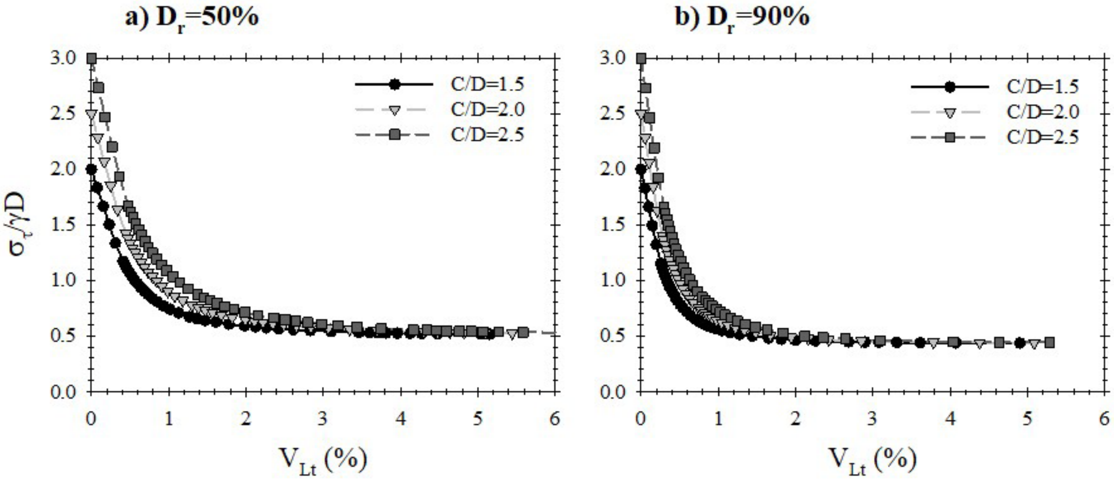

Figure 7. Normalized internal radial stress at springline versus tunnel volume loss, for C/D=1.5, 2.0 and 2.5; D_r=50% (a) and D_r=90% (b).

The normalized minimum internal radial stress depends only on the friction angle, with $\sigma_t/\gamma D$ equal to 0.52 for a relative density of 50% (friction angle of 35 degrees) and $\sigma_t/\gamma D$ equal to 0.44 for a relative density of 90% (friction angle of 39 degrees).

For a valid comparison between numerical and analytical solutions, the numerical model must match the boundary conditions of the analytical solution. For example, Vitali et al. (2024a) demonstrated excellent agreement between numerical modeling and analytical solution of Caquot (1934), later extended by Carranza-Torres et al. (2013). In this study, the minimum radial stress does not align with the solution of Atkinson & Potts (1977) due to differences in boundary conditions.

As shown in Figure 7, the minimum radial stress required to maintain stability has already been reached in all studied cases when the tunnel volume loss reaches 5%, indicating opening instability. Figure 8 presents the equivalent plastic strains that develop around the tunnel for all scenarios at 5% tunnel volume loss. The definition of equivalent plastic strain is given by Equation 1:

$$\varepsilon_p = \int \sqrt{\frac{2}{3}\dot{\varepsilon}_{ij}\dot{\varepsilon}_{ij}}\, dt \tag{1}$$

In all cases, a pronounced accumulation of plastic strain exceeding 5% is observed at the tunnel crown. This results from the boundary conditions imposed in the numerical models, which replicate those of the centrifuge tunnel tests. The observed behavior is consistent with the accumulated shear strains observed in centrifuge tests using PIV techniques (Marshall, 2009; Farrell, 2011; Zhou, 2015).

Notably, a plastic strain zone develops at the ground surface. For $C/D = 1.5$, this zone clearly connects with the plastic strain zone surrounding the tunnel, suggesting the potential for a daylight failure mechanism (Vitali et al., 2024a). However, this connection is less pronounced for $C/D = 2$ and nearly nonexistent for $C/D = 2.5$. Interestingly, although the minimum radial stress threshold is reached in all cases, the numerical models do not exhibit a distinct daylight failure mechanism.

Furthermore, at a relative density of 90%, plastic strain accumulation is more localized at the tunnel crown, whereas at a relative density of 50%, plastic strain is more widely distributed. This difference arises from the more dilatant behavior of denser sands, which enhances the arching effect of stress redistribution around the tunnel, as discussed in detail by Vitali et al., 2024b.

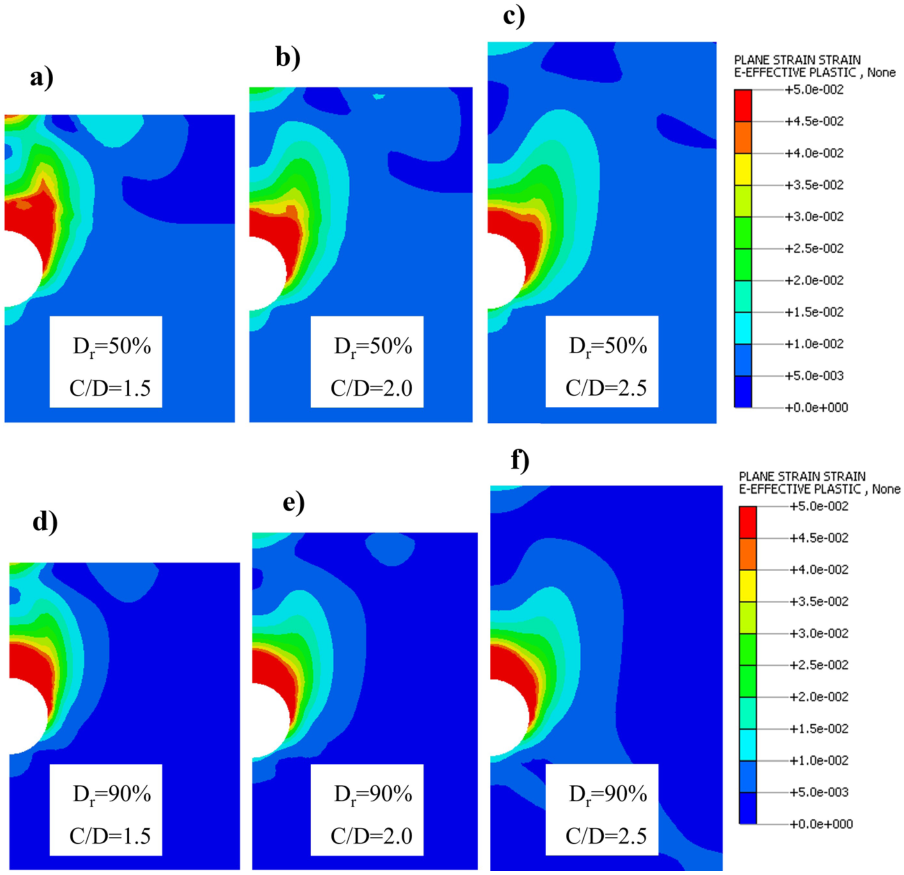

Figure 8. Equivalent plastic strain field for V_{Lt} = 5%, for the different cases.

3.2 Volumetric behavior

As discussed by Franza et al. (2019) and Vitali et al. (2024b), shallow tunnels in sandy soils exhibit complex behavior due to volumetric deformations in the ground as tunnel volume loss increases. Consequently, surface settlements and horizontal displacements, and thus the potential for damage to adjacent structures, are closely linked to the distribution of volumetric strains within the sandy soil mass.

Figure 9 illustrates the volumetric strain distribution for cover-to-diameter ratios of 1.5, 2.0, and 2.5, and relative densities of 50% and 90%, considering tunnel volume losses of 1%, 3%, and 5%. Negative volumetric strains indicate dilation, while positive values represent contraction. For a tunnel volume loss of 1%, the volumetric strains surrounding the tunnel are relatively small (i.e., mostly smaller than 0.1%). However, it is possible to observe the onset of an arch-shaped contraction zone forming above the tunnel near the surface, extending to the side of the tunnel for sandy soil with a relative density of 50%, and a dilation zone at the tunnel perimeter extending from the springline to the tunnel crown for sandy soil with a relative density of 90%.

For large tunnel volume losses (e.g., 3% and 5%), the arch-shaped contracting zone and the dilation zone at the tunnel perimeter become fully developed and well-defined. The shapes of the contraction and dilation zones are similar across the different tunnel depths studied (*C/D* = 1.5, 2.0, and 2.5); however, the volume of the arch-shaped contraction zone increases with tunnel depth, while the size of the dilation zone above the tunnel appears to be only slightly affected by tunnel depth. On the other hand, the dilation zone is significantly larger, and the arch-shaped contracting zone is considerably less pronounced for a relative density of 90% than for 50%, due to the more dilative behavior of denser sands.

The development of the dilative and contraction zones results from the arching of stresses around the opening, as

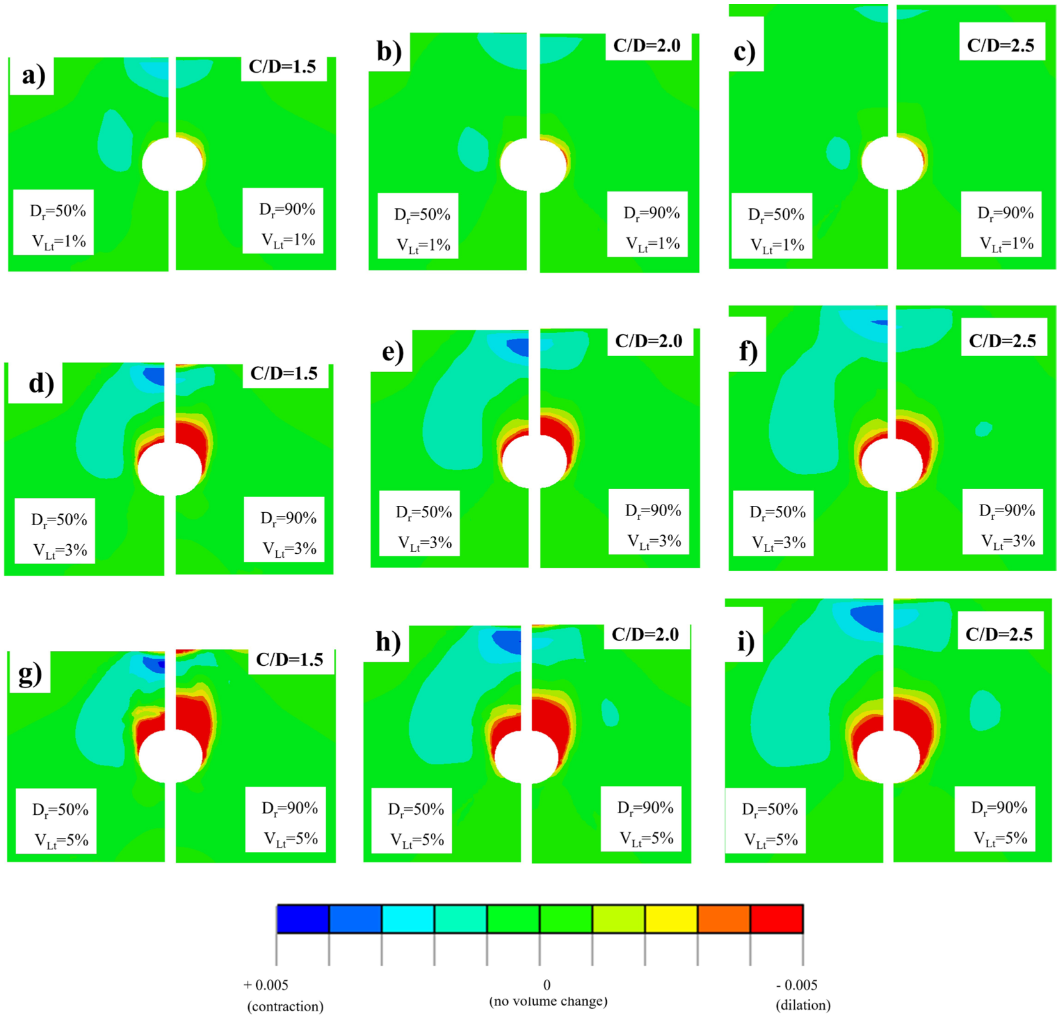

Figure 9. Volumetric strain field for tunnel volume loss equal to 1%, 3% and 5%. D_r = 50% at left and D_r = 90% at right. Dilation is represented by negative strain and contraction positive. Figures (a) to (c), (d) to (f), and (g) to (i) show tunnel volume losses of 1%, 3%, and 5%, respectively. The *C/D* ratios are divided into columns as follows: 1.5 (a, d, g), 2.0 (b, e, h), and 2.5 (c, f, i).

discussed by Vitali et al. (2024b). Within the contraction zone, the mean effective stress increases as tunnel volume loss grows due to stress redistribution, and the shear demand is low. This leads to contraction even in very dense sandy ground (i.e., relative density of 90%). Near the tunnel, the mean effective stress decreases as tunnel volume loss increases and the shear demand is high, causing dilation in this region, even in loose sands. However, the most significant factor appears to be the relative density of the sandy soil, which ultimately determines whether the overall behavior is more dilative or contractive.

Figure 10 compares tunnel volume loss (V_{Lt}) and soil volume loss (V_{Ls}) for different tunnel depths (C/D = 1.5, 2.0, and 2.5) and relative densities (Dr = 50% and 90%). The tunnel volume loss is computed based on displacements at the tunnel perimeter, while the soil volume loss is derived from the settlement trough at the surface. In tunneling practice, volume loss is typically estimated from the settlement trough since tunnel volume loss is unknown. If no volume change occurs, such as in the case of undrained behavior in saturated clays, the tunnel and soil volume losses are equal. However, in sandy soils, which undergo volumetric changes, these volume losses differ, as illustrated in Figure 9.

As shown in Figure 10, the relationship between soil and tunnel volume loss is nearly linear for small tunnel volume losses, with increments in soil volume loss exceeding those in tunnel volume loss (i.e., the tangent of the slope angle is greater than 1). Notably, for tunnel volume losses below approximately 1%, this relationship remains similar regardless of tunnel depth or relative density. As tunnel volume loss increases, the relationship becomes nonlinear, with increments in soil volume loss gradually decreasing relative to tunnel volume loss (i.e., the tangent of the slope approaches 1). Eventually, the increments in soil volume loss become smaller than those in tunnel volume loss (i.e., the tangent of the slope falls below 1). This transition occurs because, as tunnel volume loss increases, a dilation zone develops around the tunnel perimeter and expands in size and intensity, eventually leading to an overall dilative volumetric response of the sandy ground. For larger tunnel volume losses, tunnel depth, and soil relative density significantly influence the relationship between soil and tunnel volume loss. The shallower the tunnel and the denser the sandy soil, the more pronounced the dilative response of the ground.

3.3 Vertical displacements profile

The vertical displacements along the tunnel centerline above the tunnel crown for all studied scenarios (i.e., C/D =1.5, 2 and 2.5 and relative densities of 50 and 90%) are analyzed in this section. Figures 11a, c, e show the surface settlement to crown displacement ratio ($S_{v,s}/S_{v,crown}$) with tunnel volume loss (V_{Lt}) and Figures 11b, d, f, the normalized vertical displacements (S_v/R) with depth along the tunnel centerline for V_{Lt} = 1, 3, and 5%.

As shown in Figure 11, for tunnel volume losses smaller than 1%, the ratio $S_{v,s}/S_{v,crown}$, as well as the vertical displacement profiles observed for relative densities of 50% and 90%, follow the same trend regardless of tunnel depth, however the absolute values of $S_{v,s}/S_{v,crown}$ decrease as the relative depth increases. This is consistent with Figure 10, which shows that the evolution of tunnel and soil volume losses is similar when tunnel volume loss is small. As discussed in the previous section, the development of a

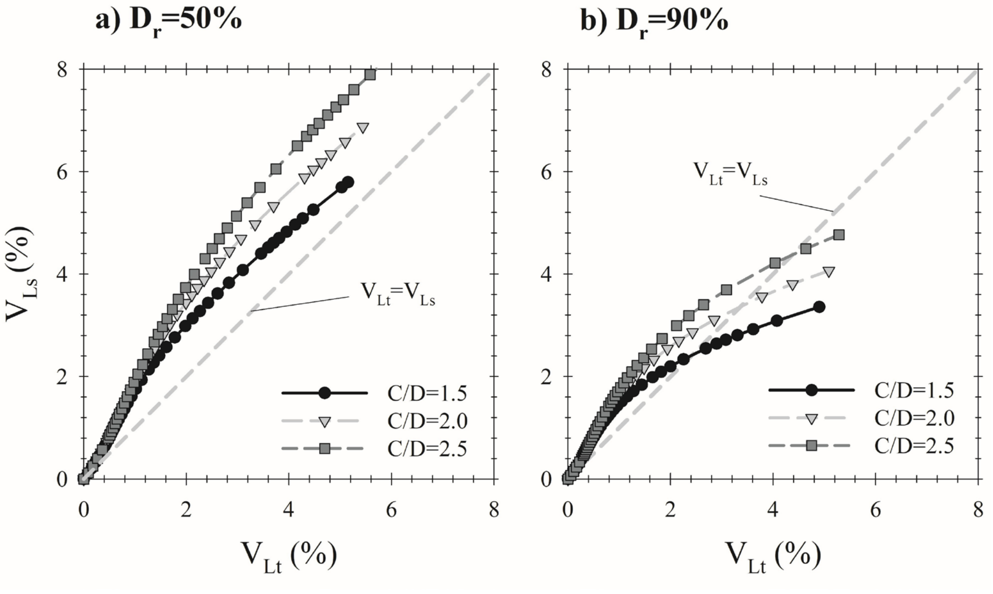

Figure 10. Soil volume loss versus tunnel volume loss, for C/D = 1.5, 2.0 and 2.5; D_r = 50% (a) and D_r = 90% (b).

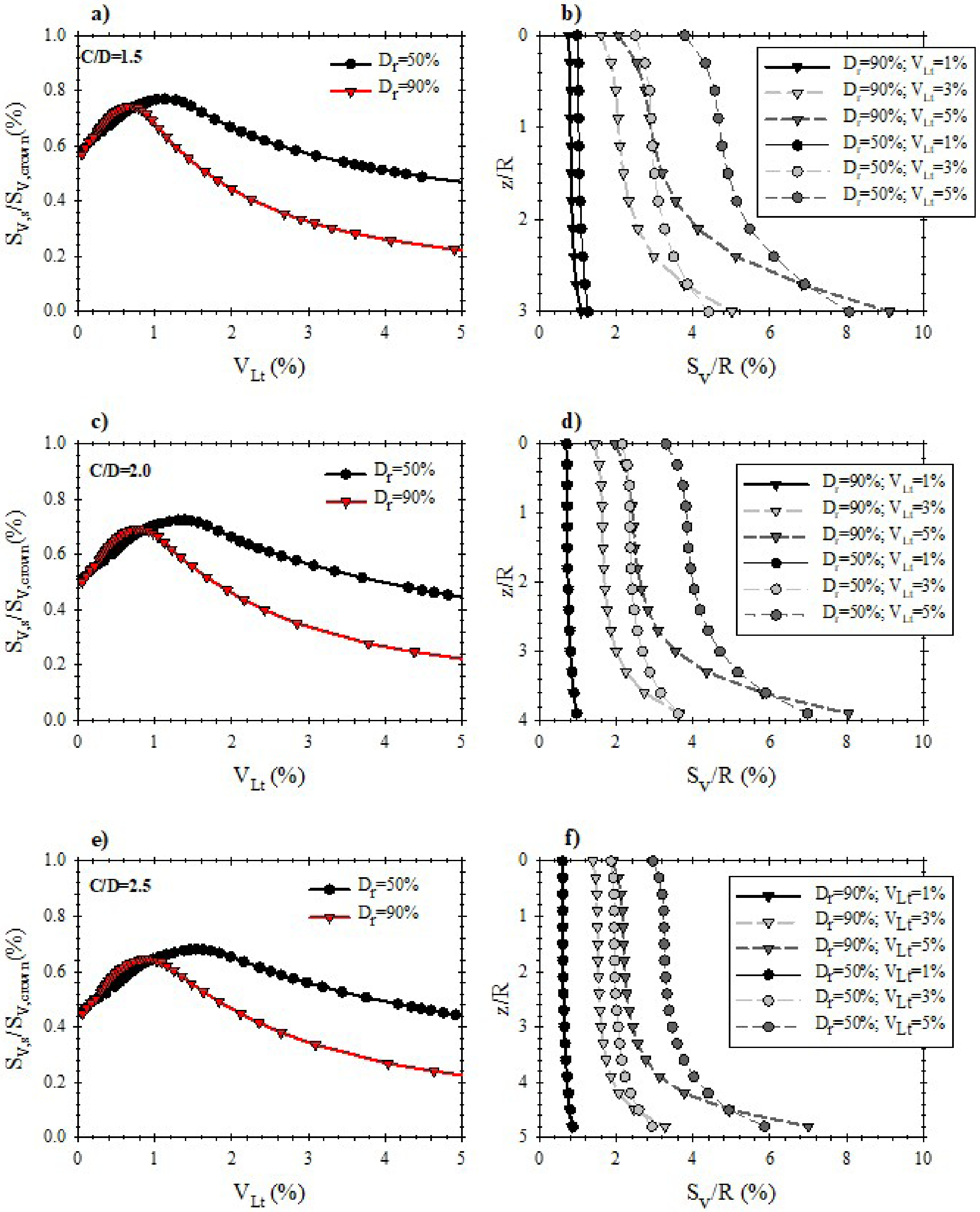

Figure 11. (a, c, e) Ratio between vertical displacements at the ground surface and the tunnel crown with tunnel volume loss; (b, d, f) Normalized vertical displacements versus depth for tunnel volume losses of 1, 3 and 5%. Results for *C/D* = 1.5 (a, b), 2.0 (c, d) and 2.5 (e, f). The tunnel radius is equal to 5m (i.e., *R* = 5 m).

dilative zone around the tunnel perimeter and the transition from contractive to dilative ground behavior require relatively large tunnel volume losses. For tunnel volume losses below 1%, this transition has not yet occurred.

As shown in Figures 11a, 11c, and 11e, the ratio $S_{v,s}/S_{v,crown}$ increases with tunnel volume loss, reaching a maximum value before gradually decreasing as tunnel volume loss continues to increase. This trend is associated with the development of the dilation zone surrounding the tunnel perimeter, which facilitates stress arching and consequently reduces ground deformations reaching the surface, as discussed by Vitali et al. (2024b). Thus, the observed peak in the ratio $S_{v,s}/S_{v,crown}$ is linked to the formation of the dilation zone around the tunnel perimeter. As shown in Figure 11, the tunnel volume loss corresponding to the maximum ratio $S_{v,s}/S_{v,crown}$ decreases as the sandy soil becomes denser and the tunnel becomes shallower.

Furthermore, Figures 11b, d, and f show that vertical displacements with depth along the tunnel centerline exhibit little variation for small volume losses (i.e., 1%). However, the settlement rapidly increases at depths approaching the tunnel crown for large values of tunnel volume loss (e.g., 3% and 5%). The displacement pattern and significant variation at the tunnel crown are consistent with volumetric strain zones (see Figure 9).

As shown, the volumetric changes in the ground significantly affect how deformations propagate to the surface. From a tunneling engineering perspective, this reinforces the importance of instrumentation readings near the tunnel crown, using devices such as profilometers and deep settlement devices. Meanwhile, surface benchmark readings are directly impacted by volumetric variations in the ground, emphasizing the need for a comprehensive monitoring strategy.

3.4 Surface displacements

Figure 12 presents the settlements and horizontal displacements at the ground surface as a function of the distance from the tunnel centerline, x, for all studied cases. These cases include cover-to-diameter (C/D) ratios of 1.5, 2.0, and 2.5, with a relative density of 50% shown on the left side of the graphs and 90% on the right side. The presented displacements correspond to tunnel volume losses of 1%, 3%, and 5%.

For small tunnel volume losses (1%), both horizontal and vertical displacements are relatively small and show little variation between soil relative densities. This is consistent with the discussion in previous sections. As tunnel volume loss increases, the displacements at the ground surface also increase, and the differences in vertical and horizontal displacements between relative densities of 50% and 90% become more pronounced.

Deeper tunnels (e.g., $C/D = 2.5$) exhibit wider settlement troughs and smaller maximum surface displacements compared to shallower tunnels (e.g., $C/D = 1.5$). Thus, deeper tunnels are less likely to cause damage to adjacent structures than shallower tunnels.

In tunneling engineering practice, horizontal displacements are often estimated from vertical displacements by assuming the direction of the displacement vector. The horizontal displacement can then be determined using the following Equation 2:

$$S_h = S_v \cdot x / Z_v \tag{2}$$

where S_h and S_v represent horizontal and vertical displacements, x is the offset from the tunnel centerline, and Z_v is the depth

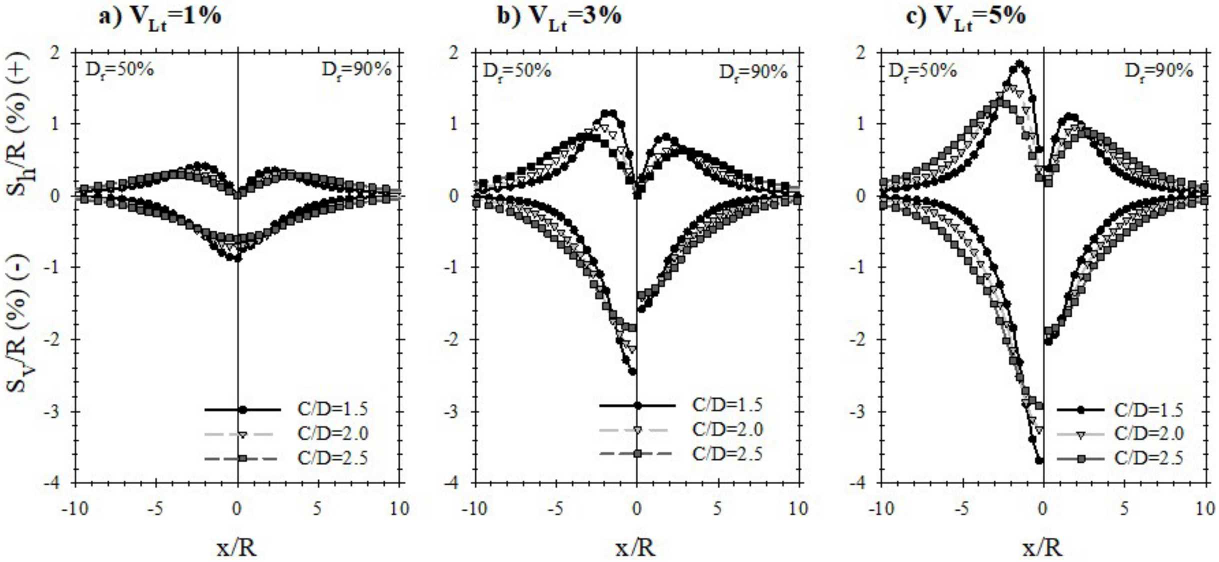

Figure 12. Normalized vertical and horizontal displacements, at the ground surface versus the normalized distance from the tunnel centerline. Tunnel volume loss of 1% (a), 3% (b) and 5% (c), for C/D = 1.5, 2.0 and 2.5; D_r = 50% (left) and D_r = 90% (right). The tunnel radius is equal to 5m (i.e., R = 5 m).

at which the trajectory of the displacement vector intersects the tunnel centerline, as shown in Figure 13a.

O'Reilly & New (1982) suggested that, under constant volume conditions, the displacement vector of any point on the ground surface at a distance *x* from the tunnel centerline points toward the tunnel's center (i.e., $Z_v = Z_t$).

Figures 13b and 13c show the variation of Z_v with *x*, both normalized by Z_t and *R*, respectively. The results are shown up to absolute values of *x/R* equal to 6, beyond which vertical and horizontal displacements are small and irrelevant to above ground structures.

Notably, the ratio Z_v/Z_t is always less than 1, indicating that the displacement vector trajectory intersects the tunnel centerline above the tunnel's center. As a reference, the relative depth Z_v/Z_t at the tunnel crown equals 0.75, 0.8, and 0.83 for cover-to-diameter ratios (*C/D*) of 1.5, 2.0, and 2.5, respectively.

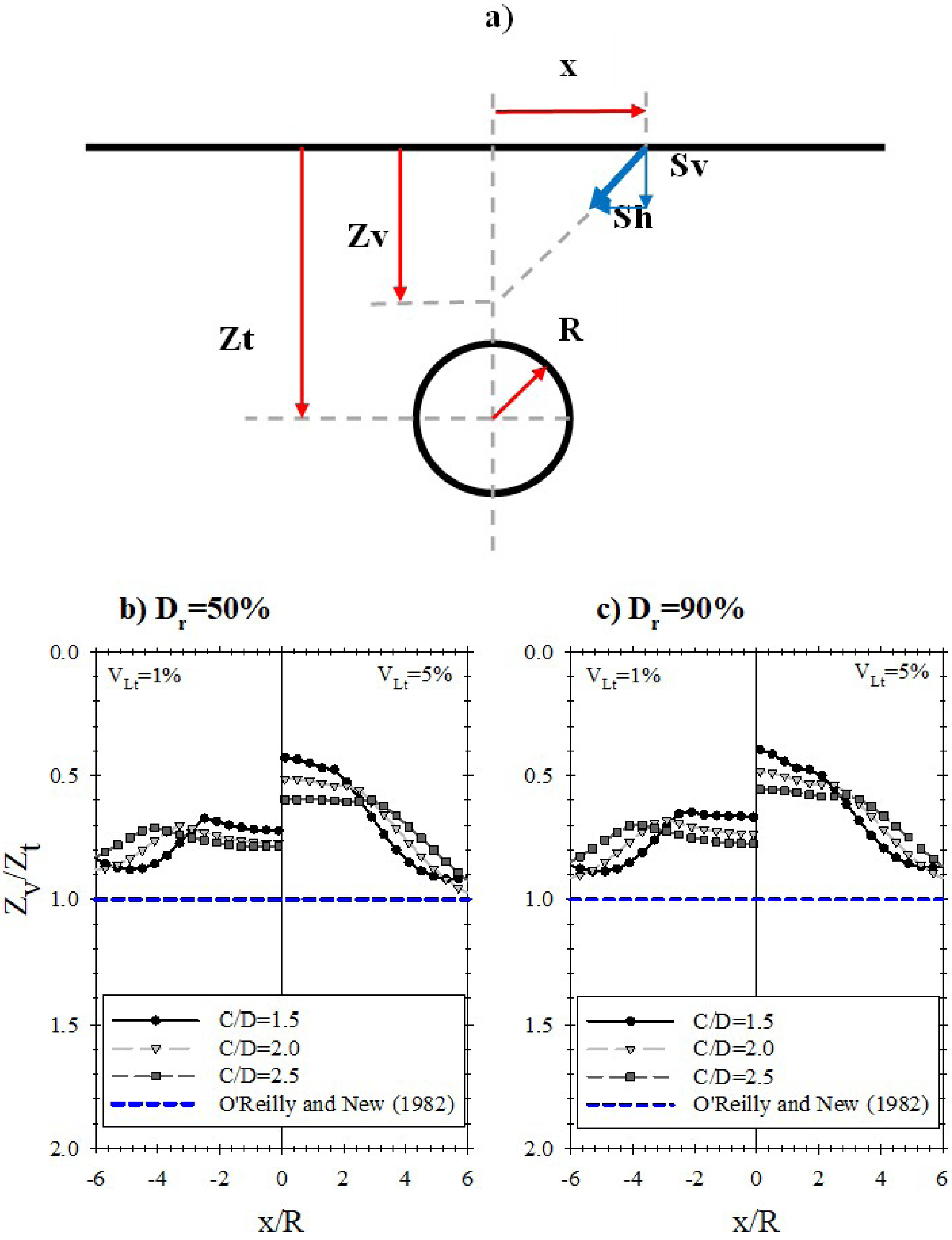

Figure 13. Normalized intersection depth, Z_v, with respect to the tunnel depth, Z_t, versus normalized distance from the tunnel center line, *x/R*. Tunnel volume loss equal to 1% (left) and 5% (right), for *C/D* = 1.5, 2.0 and 2.5; D_r = 50% b) and D_r = 90% (c). Comparison with O'Reilly & New (1982). The tunnel radius is equal to 5 m (i.e., *R* = 5 m).

Additionally, the intersection depth Z_v varies significantly with the distance from the tunnel centerline, x, the soil relative density D_r, the cover-to-diameter ratio C/D, and the tunnel volume loss V_{Lt}. The numerical modeling results indicate that assuming a constant Z_v/Z_t ratio to predict horizontal displacements based on settlement may lead to inaccurate predictions in sandy ground.

Predicting horizontal displacements is crucial for assessing damage to aboveground structures. As shown in Figure 13, it is difficult to directly relate horizontal displacements to vertical ones, as various factors influence this relationship. The next section presents a correlation between horizontal strain and angular distortions at the ground surface. Vitali et al. (2024b) demonstrated that estimating the horizontal strains directly from the angular distortion at the surface is a more effective approach for predicting the potential for building damage.

3.5 Potential damage in structures

Assessing the potential for structural damage to adjacent structures due to tunnel excavation is a critical and complex stage in tunnel design. Predictions depend on various factors, such as the geomechanical behavior of the soil mass, excavation geometry, construction sequence, tunnel depth, structural stiffness, conditions of the adjacent structures, and foundation type of adjacent buildings. Given the complexity of the analysis, a staged approach to damage assessment is a more reasonable practice in tunnel design. It begins with a greenfield assessment and increases in complexity only if necessary (e.g., incorporating adjacent structures in the numerical modeling of the tunnel excavation).

Currently, tunnel design heavily relies on numerical modeling, allowing for a complete prediction of displacements and strain fields. Vertical and horizontal displacements obtained under greenfield conditions may be used for preliminary assessment of potential damage to adjacent structures. Assuming that a structure deforms according to greenfield conditions is a conservative and practical approach for preliminary analyses, especially given the uncertainties present in the early design stages. This assumption ensures that potential deformation effects are not underestimated, allowing for safer initial assessments before more refined evaluations are conducted. Rigid structures tend to deform more uniformly, and depending on the foundation type, such as a raft foundation, horizontal deformations may become negligible. It is important to highlight that vulnerable and historic structures, due to simpler construction methods, typically tend to deform under greenfield conditions.

Given both vertical and horizontal displacements, the Son & Cording (2005) criterion provides a practical method for assessing potential surface damage. This approach considers the principal strain (ε_p), directly correlating angular distortion (β) with horizontal strain (ε_h), and there is no need for structure parameters, as shown in Equation 3:

$$\varepsilon_p = \varepsilon_h \cos^2\theta_{max} + \beta \sin\theta_{max} \cos\theta_{max} \tag{3}$$

where θ_{max} is given by $\tan 2\theta_{\max} = \left|\beta / \varepsilon_{\mathrm{h}}\right|$.

Using Equation 3, it is possible to quickly determine the maximum principal strains. Son & Cording (2005) also define structural damage levels based on principal strain values. In this study, three damage intervals will be used as reference:

I. Slight to Moderate: $0.075\% < \varepsilon_p < 0.167\%$
II. Moderate to Severe: $0.167\% < \varepsilon_p < 0.333\%$
III. Severe to Very Severe: $\varepsilon_p > 0.333\%$

Figure 14 shows the evolution of the maximum principal strain at the ground surface as tunnel volume loss increases for different cover-to-diameter ratios (C/D = 1.5, 2.0, and 2.5) and relative densities of 50% (Figure 14a) and 90% (Figure 14b). The damage classification ranges proposed by Son & Cording (2005) are also indicated. Figures 14c and 14d present the normalized distance from the tunnel centerline, x/Z_t, where maximum principal strain ($\varepsilon_{p,max}$) occurs with the tunnel volume loss for the same cases.

As shown, for a relative density of 50% (medium-dense sandy soil), the principal strain evolves almost linearly with tunnel volume loss. In contrast, for a relative density of 90% (dense sand), the principal strain exhibits a slightly nonlinear evolution as the tunnel volume loss (V_{Lt}) increases due to dilatancy effects, as discussed in previous sections.

The potential for structural damage is significantly lower at higher relative densities and greater depths. Notably, even under large tunnel volume losses in medium dense sand (i.e., D_r=50%), for C/D=2.5, the accumulated principal strain does not reach the damage category III, highlighting the potential to avoid surface damage by increasing the tunnel depth.

Regarding the location of the maximum principal strain, $\varepsilon_{p,max}$, Figures 14c and 14d show that the normalized distance from the tunnel centerline with respect to the tunnel depth, x/Z_t, where $\varepsilon_{p,max}$ occurs, is only slightly affected by the sandy soil relative density (D_r) and the cover-to-diameter ratio (C/D). However, it is influenced by tunnel volume loss. As shown, the location of the maximum principal strain tends to shift closer to the tunnel centerline as the tunnel volume loss increases. For small tunnel volume losses, x/Z_t ranges from 0.9 to 1.2, whereas for large tunnel volume losses, it ranges from 0.6 to 0.8.

Figure 15 presents the relationship between angular distortion and horizontal strain corresponding to the maximum principal strain at the ground surface for the investigated cases in this study (C/D = 1.5, 2.0, and 2.5; D_r = 50% and 90%). The graph also includes the damage classification zones proposed by Son & Cording (2005), the reference from Vitali et al. (2024b) based on the NorSand model, which suggests a direct relationship between angular distortion and horizontal strain (ε_h=0.67β) and the relationship suggested by the results in this study (ε_h=0.77β). The results obtained in this study reveal a nearly linear trend, even for high tunnel volume losses, closely matching the predictions by Vitali et al. (2024b).

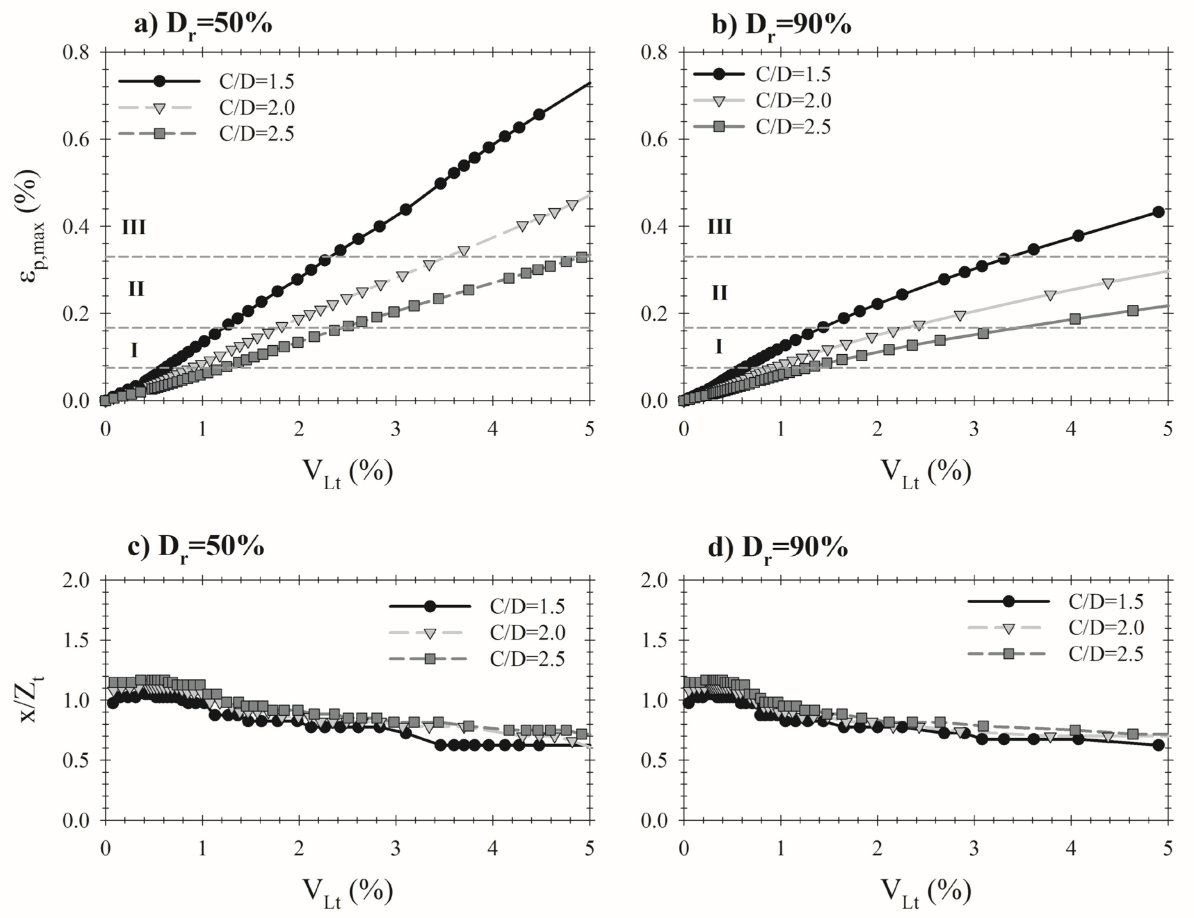

Figure 14. Maximum principal strain ($\varepsilon_{p,max}$) at the ground surface (*a* and *b*) and normalized distance to the tunnel centerline with respect to the tunnel depth (x/Z_t) where $\varepsilon_{p,max}$ occur (*c* and *d*) versus tunnel volume loss, for *C*/*D* = 1.5, 2.0 and 2.5; D_r = 50% (*a* and *c*) and D_r = 90% (*b* and *d*).

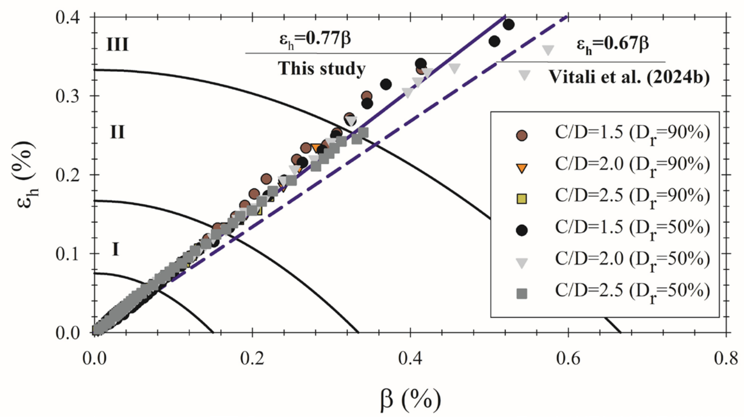

Figure 15. Horizontal strain and angular distortions corresponding to the maximum principal strain at the ground surface. Regions I, II, and III correspond to slight, moderate to severe, and severe to very severe damage.

This direct correlation simplifies the inclusion of horizontal strain in damage assessments. As shown earlier, predicting horizontal displacements from vertical ones alone is challenging due to various influencing factors. In tunneling practice, vertical displacements are typically measured and approximated using empirical functions like the Gaussian (Peck, 1969; Schmidt, 1969) or the Yield Density curve (Celestino & Ruiz, 1998; Celestino et al., 2000). Incorporating the horizontal strain into damage evaluation can be done by following the practical steps:

i. Fit the settlement trough using an appropriate function (e.g., Yield Density),
ii. Calculate angular distortions along the surface;
iii. Identify angular distortions at $x/Z_t \approx 0.7$ to 1 and estimate horizontal strain using ε_h=0.72β (average from this study and Vitali et al., 2024b).
iv. Compute the principal strain (Equation 2) and classify the potential damage. Another possibility is to directly input the angular distortion value in Figure 15, eliminating step iii.

4. Conclusions

This study presents a comprehensive investigation of shallow tunnel behavior in sandy ground using numerical modeling that replicates centrifuge tunnel tests. The numerical modeling approach was validated through comparisons with three centrifuge tunnel tests. The numerical models accurately replicated the observed deformation patterns and settlements, closely matching centrifuge test results at varying tunnel depths, diameters, and sand relative densities for tunnel volume losses up to 5%. With the calibrated model, a set of numerical experiments was performed to investigate the behavior of shallow tunnels in cohesionless soil.

It was observed that the minimum internal radial stress required for stability is independent of the tunnel depth. This aligns with Atkinson & Potts's (1977) analytical solution. However, differences in boundary conditions between numerical and analytical solutions must be carefully considered to ensure valid comparisons.

The numerical experiment results show that the soil volumetric response is strongly influenced by tunnel volume loss, tunnel depth, and soil relative density. The numerical experiments show that the sandy ground behavior remains predominantly contractive for small tunnel volume losses, with soil volume loss exceeding tunnel volume loss even in dense sands for tunnel volume losses (V_{Lt}) up to about 1%. However, as tunnel volume loss increases, the overall volumetric behavior gradually transitions from contractive to dilative for the relative densities studied (50% and 90%). Two distinct zones develop: an arch-shaped contraction zone extending from the ground surface to the tunnel springline and a dilative zone above the tunnel crown. These zones are associated with stress arching around the opening and are influenced by tunnel volume loss, tunnel depth, and soil relative density.

Volumetric strains influence the displacements above the tunnel, with contraction and dilation zones significantly affecting how excavation-induced stress relief manifests at the surface. From a tunneling engineering perspective, this underscores the importance of instrumentation near the tunnel crown, using devices such as profilometers and deep settlement devices. Meanwhile, surface benchmark readings are directly affected by volumetric variations in the ground, highlighting the need for a comprehensive monitoring strategy.

Numerical modeling results demonstrate that the depth at which the displacement vector intersects the tunnel centerline (Z_v) varies with tunnel depth, relative density, distance from the tunnel centerline, and tunnel volume loss. The numerical results indicate that assuming a displacement vector trajectory intersecting the tunnel centerline at a fixed Z_v can lead to inaccuracies in estimating horizontal displacements from surface settlements.

The findings of this study support the strong correlation observed by Vitali et al. (2024b) between angular distortion and horizontal strain at the location of maximum principal strain on the ground surface. The nearly linear trend observed simplifies the incorporation of horizontal strain into damage assessments. This study presents a practical approach for estimating horizontal strain by leveraging well-established empirical settlement functions (e.g., the Yield Density function, Celestino & Ruiz, 1998; Celestino et al., 2000) and derived angular distortions. These results contribute to refining damage prediction methods, offering a more reliable approach for integrating horizontal strain effects into damage assessments.

The findings of this research should not be extrapolated beyond the assessed scenarios. For different conditions, the approach presented in this paper is recommended, which involves rigorously calibrating soil behavior using an advanced constitutive model based on high-quality laboratory or field data, along with a detailed numerical modeling approach following well-established procedures.

Acknowledgements

The authors acknowledge the support provided by the research funding agency of the Brazilian Government, CNPq (Conselho Nacional de Desenvolvimento Cientifico e Tecnológico), Contract 162113/2020- 0: Post-Doctoral Scholarship, and CAPES (Coordenação de Aperfeiçoamento de Pessoal de Nível Superior): Scholarship for Master's Program. The authors also thank the Midas Information Technology Co., Ltd. for providing the license for the Midas GTS NX software used in this research.

Declaration of interest

The authors have no conflicts of interest to declare. All co-authors have observed and affirmed the contents of the paper and there is no financial interest to report.

Authors' contributions

Tarcisio Barreto Celestino: conceptualization, data curation, methodology, supervision, validation, writing – original draft. writing – review & editing. Felipe Paiva Magalhães Vitali: conceptualization, data curation, formal analysis, methodology. Osvaldo Paiva Magalhães Vitali: conceptualization, data curation, methodology, supervision, validation, writing – review & editing.

Data availability

The datasets generated and analyzed in the course of the current study are available from the corresponding author upon request.

Declaration of use of generative artificial intelligence

This work was prepared without the assistance of any generative artificial intelligence (GenAI) tools or services. All aspects of the manuscript were developed solely by the authors, who take full responsibility for the content of this publication.

List of symbols

c	Cohesion
m	Power for stress-level dependency of stiffness
q	Deviatoric stress
z	Depth
C	Cover
D	Diameter
Dr	Relative density
E_{50}	Secant Young's modulus in standard drained triaxial test
E_{oed}	1D compression modulus for primary oedometer loading
E_{ur}	Unloading/reloading Young's modulus
$K_{0,NC}$	K_0-value for normal consolidation
OCR	Overconsolidation ratio
P_{ref}	Reference stress for stiffness
R	Radius
R_f	Failure ratio
S_h	Horizontal displacement
S_v	Vertical displacement
V_{Ls}	Soil volume loss
V_{Lt}	Tunnel volume loss
β	Angular distortion
γ	Unit weight
ε_{ax}	Axial strain
ε_{h}	Horizontal strain
ε_{p}	Principal strain
ε_{p}	Equivalent plastic strain
ε_{vol}	Volumetric strain
ν_{ur}	Poisson's ratio for unloading/reloading
σ_t	Tunnel pressure – radial stress
φ	Friction angle
Ψ	Dilatancy angle

References

Atkinson, J.H., & Potts, D.M. (1977). Stability of a shallow circular tunnel in cohesionless soil. *Geotechnique*, 27(2), 203-215. http://doi.org/10.1680/geot.1977.27.2.203.

Boldini, D., Losacco, N., Franza, A., DeJong, M.J., Xu, J., & Marshall, A.M. (2021). Tunneling-induced deformation of bare frame structures on sand: numerical study of building deformations. *Journal of Geotechnical and Geoenvironmental Engineering*, 147(11), 438. http://doi.org/10.1061/(ASCE)GT.1943-5606.0002627.

Caquot, A. (1934). Équilibre des massifs a frottement interne. Gauthier-Villars.

Carranza-Torres, C., Reich, T., & Saftner, D. (2013). Stability of shallow circular tunnels in soils using analytical and numerical models. In *Proceedings of the 61st Minnesota Annual Geotechnical Engineering Conference*. Falcon Heights: University of Minnesota.

Celestino, T.B., & Ruiz, A.P.T. (1998). Shape of settlement throughs due to tunneling through different types of soft ground. *Felsbau*, 16, 118-121.

Celestino, T.B., Gomes, R.A.M., & Bortuluci, A.A. (2000). Errors in ground distortions due to settlement through adjustment. *Tunnelling and Underground Space Technology*, 15(1), 97-100. http://doi.org/10.1016/S0886-7798(99)00054-1.

Farrell, R.P. (2011). *Tunnelling in sands and the response of buildings* [Doctoral thesis]. University of Cambridge, Cambridge, UK.

Franza, A. (2016). *Tunnelling and its effects on piles and piled structures* [Doctoral thesis]. University of Nottingham, Nottingham, UK.

Franza, A., Marshall, A.M., & Zhou, B. (2019). Greenfield tunnelling in sands: the effects of soil density and relative depth. *Geotechnique*, 69(4), 297-307. http://doi.org/10.1680/jgeot.17.P.091.

Giardina, G., DeJong, M.J., & Mair, R.J. (2015). Interaction between surface structures and tunnelling in sand: centrifuge and computational modelling. *Tunnelling and Underground Space Technology*, 50, 465-478. http://doi.org/10.1016/j.tust.2015.07.016.

Giardina, G., Losacco, N., DeJong, M.J., Viggiani, G.M., & Mair, R.J. (2019). Effect of soil models on the prediction of tunnelling-induced deformations of structures. *Geotechnical Engineering*, 173(5), 379-397. http://doi.org/10.1680/jgeen.18.00127.

Jefferies, M.G. (1993). Nor-Sand: a simple critical state model for sand. *Geotechnique*, 43(1), 91-103. http://doi.org/10.1680/geot.1993.43.1.91.

Lanzano, G., Visone, C., Bilotta, E., & Santucci de Magistris, F. (2016). Experimental assessment of the stress–strain behaviour of leighton buzzard sand for the calibration of a constitutive model. *Geotechnical and Geological Engineering*, 34(4), 991-1012. http://doi.org/10.1007/s10706-016-0019-5.

Mair, R.J., Taylor, R.N., & Bracegirdle, A. (1993). Subsurface settlement profiles above tunnels in clay. *Geotechnique*, 43(2), 315-320. http://doi.org/10.1680/geot.1993.43.2.315.

Marshall, A. (2009). *Tunnelling in sand and its effect on pipelines and piles* [Doctoral thesis]. University of Cambridge, Cambridge, UK.

O'Reilly, M.P., & New, B.M. (1982). Settlements above tunnels in the United Kingdom - their magnitude and prediction. In *Tunnelling '82, Papers Presented at the 3rd International Symposium*. London: Inst of Mining and Metallurgy.

Peck, B. B. (1969). Deep excavation and tunnelling in soft ground, State of the art volume. In *Proceedings of the 7th ICSMFE* (Vol. 4, pp. 225-290). Mexico City.

Ritter, S. (2018). *Experiments in tunnel-soil-structure interaction* [Doctoral thesis]. University of Cambridge, Cambridge, UK.

Schmidt, B. (1969). *Settlements and ground movements associated with tunneling in soil*. University of Illinois at Urbana-Champaign.

Son, M., & Cording, E.J. (2005). Estimation of building damage due to excavation-induced ground movements. *Journal of Geotechnical and Geoenvironmental Engineering*, 131(2), 162-177. http://doi.org/10.1061/(ASCE)1090-0241(2005)131:2(162).

Vitali, F.P.M., Vitali, O.P.M., Celestino, T.B., & Bobet, A. (2024a). FEM modeling requirements for accurate highly nonlinear shallow tunnels analysis. *Soil and Rocks*, 47(1), e2024000923. http://doi.org/10.28927/SR.2024.000923.

Vitali, F.P.M., Vitali, O.P.M., Celestino, T.B., & Bobet, A. (2024b). Numerical analysis of relative density effects on shallow TBM tunnel excavation: ground behavior and principal strains at surface in greenfield conditions. *Tunnelling and Underground Space Technology*, 154, 106104. http://doi.org/10.1016/j.tust.2024.106104.

Vitali, F.P.M., Vitali, O.P.M., & Celestino, T.B. (September 24-27, 2024c). Influence of tunnel depth on ground response in loose and dense sandy soils in urban environments. In *Proceedings of COBRAMSEG2024* (pp. 1-8). Balneário Camboriú/SC. http://doi.org/10.47094/COBRAMSEG2024/713.

Vitali, O.P.M., Celestino, T.B., & Bobet, A. (2018a). 3D finite element modeling optimization for deep tunnels with material nonlinearity. *Underground Space*, 3(2), 125-139. http://doi.org/10.1016/j.undsp.2017.11.002.

Vitali, O.P.M., Celestino, T.B., & Bobet, A. (2018b). Analytical solution for tunnels not aligned with geostatic principal stress directions. *Tunnelling and Underground Space Technology*, 82, 394-405. http://doi.org/10.1016/j.tust.2018.08.046.

Vitali, O.P.M., Celestino, T.B., & Bobet, A. (2019a). Shallow tunnel not aligned with the geostatic principal stress directions. In *Proceedings of Geo-Congress2019 GSP 313* (pp. 214-222). USA: ASCE. http://doi.org/10.1061/9780784482155.023.

Vitali, O.P.M., Celestino, T.B., & Bobet, A. (2019b). Shallow tunnels misaligned with geostatic principal stress directions: analytical solution and 3D face effects. *Tunnelling and Underground Space Technology*, 89, 268-283. http://doi.org/10.1016/j.tust.2019.04.006.

Vitali, O.P.M., Celestino, T.B., & Bobet, A. (2019c). Progressive failure due to tunnel misalignment with geostatic principal stresses. In *Proceedings of ISRM 14th International Congress on Rock Mechanics* (pp. 2292-2299). Foz do Iguassu, Brasil.

Vitali, O.P.M., Celestino, T.B., & Bobet, A. (2019d). Buoyancy effect on shallow tunnels. *International Journal of Rock Mechanics and Mining Sciences*, 114, 1-6. http://doi.org/10.1016/j.ijrmms.2018.12.012.

Vitali, O.P.M., Celestino, T.B., & Bobet, A. (2020a). Analytical solution for a deep circular tunnel in anisotropic ground and anisotropic geostatic stresses. *Rock Mechanics and Rock Engineering*, 53(9), 3859-3884. http://doi.org/10.1007/s00603-020-02157-5.

Vitali, O.P.M., Celestino, T.B., & Bobet, A. (2020b). Tunnel misalignment with geostatic principal stress directions in anisotropic rock masses. *Soils and Rocks*, 43(1), 123-138. http://doi.org/10.28927/SR.431123.

Vitali, O.P.M., Celestino, T.B., & Bobet, A. (2020c). Deformation patterns and 3D face effects of tunnels misaligned with the geostatic principal stresses in isotropic and anisotropic rock masses. In *Proceedings of 54th US Rock Mechanics /Geomechanics Symposium (ARMA 2020)*. Golden, Colorado, USA.

Vitali, O.P.M., Celestino, T.B., & Bobet, A. (2021a). New modeling approach for tunnels under complex ground and loading conditions. *Soils and Rocks*, 44(1), 1-8. http://doi.org/10.28927/SR.2021.052120.

Vitali, O.P.M., Celestino, T.B., & Bobet, A. (2021b). Behavior of tunnels excavated with dip and against dip. *Underground Space*, 6(6), 709-717. http://doi.org/10.1016/j.undsp.2021.04.001.

Vitali, O.P.M., Celestino T.B., & Bobet, A. (2022a). Construction strategies for a NATM tunnel in São Paulo, Brazil, in residual soil. *Underground Space*, 7(1), 1-18. http://doi.org/10.1016/j.undsp.2021.04.002.

Vitali, O.P.M., Celestino, T.B., & Bobet, A. (2022b). 3D face effects of tunnels misaligned with the principal directions of material and stress anisotropy. *Tunnelling and Underground Space Technology*, 122, 104347. http://doi.org/10.1016/j.tust.2021.104347.

Vorster, T.E.B. (2006). *Effects of tunnelling on buried pipes* [Doctoral thesis]. University of Cambridge, Cambridge, UK.

Xu, J., Franza, A., Marshall, A.M., Losacco, N., & Boldini, D. (2021). Tunnel–framed building interaction: comparison between raft and separate footing foundations. *Geotechnique*, 71(7), 631-644. http://doi.org/10.1680/jgeot.19.P.393.

Zhou, B. (2015). *Tunnelling-induced ground displacements in sand* [Doctoral thesis]. University of Nottingham, Nottingham, UK.